Site-Specific Imaging of Elemental Steps in Dehydration of Diols on $TiO_2(110)$

Danda P. Acharya,[†,⊥,§] **Yeohoon Yoon,**[†,§] **Zhenjun Li,**[†] **Zhenrong Zhang,**[‡] **Xiao Lin,**[†,||] **Rentao Mu,**[†] **Long Chen,**[†] **Bruce D. Kay,**[†] **Roger Rousseau,**[†,*] **and Zdenek Dohnálek**[†,*]

[†]Fundamental and Computational Sciences Directorate and Institute for Integrated Catalysis, Pacific Northwest National Laboratory, P.O. Box 999, Richland, Washington 99352, United States and [‡]Department of Physics, Baylor University, One Bear Place 97316, Waco, Texas 76798-7316, United States. [§]D. P. Acharya and Y. Yoon contributed equally. [⊥]Present address: D. P. Acharya: GlobalFoundries, 400 Stone Break Extension, Malta, New York 12020, United States. [||]Present address: X. Lin: School of Physics, University of Chinese Academy of Sciences, Beijing, 100049; and Institute of Physics, Chinese Academy of Sciences, P.O. Box 603, Beijing, 100190, People's Republic of China.

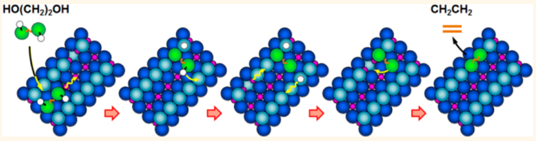

ABSTRACT Scanning tunneling microscopy is employed to follow elemental steps in conversion of ethylene glycol and 1,3-propylene glycol on partially reduced $TiO_2(110)$ as a function of temperature. Mechanistic details about the observed processes are corroborated by density functional theory calculations. The use of these two diol reactants allows us to compare and contrast the chemistries of two functionally similar molecules with different steric constraints, thereby allowing us to understand how molecular geometry may influence the observed chemical reactivity. We find that both glycols initially adsorb on Ti sites, where a dynamic equilibrium between molecularly bound and deprotonated species is observed. As the diols start to diffuse along the Ti rows above 230 K, they irreversibly dissociate upon encountering bridging oxygen vacancies. Surprisingly, two dissociation pathways, one *via* O—H and the other *via* C—O bond scission, are observed. Theoretical calculations suggest that the differences in the C—O/O—H bond breaking processes are the result of steric factors enforced upon the diols by the second Ti-bound OH group. Above ∼400 K, a new stable intermediate centered on the bridging oxygen (O_b) row is observed. Combined experimental and theoretical evidence shows that this intermediate is most likely a new dioxo species. Further annealing leads to sequential C—O_b bond cleavage and alkene desorption above ∼500 K. Simulations demonstrate that the sequential C—O_b bond breaking process follows a homolytic diradical pathway, with the first C—O_b bond breaking event accompanied with a nonadiabatic electron transfer within the $TiO_2(110)$ substrate.

KEYWORDS: titanium dioxide · diols · scanning tunneling microscopy · adsorbate dynamics · dehydration

TiO_2 is well recognized as a highly versatile catalyst with applications in diverse areas including heterogeneous catalysis, photocatalysis, solar cells, gas sensors, white pigments in paints and cosmetic products, optical and antibacterial coatings, and others.[1−3] Additionally, it has been also widely employed in studies that focus on biomass conversion and utilization.[4−12] In this context TiO_2 has shown promise both as the primary catalytic material and as the active support for metal and metal oxide clusters. Specifically, such systems have been shown to be effective in hydrogenation reactions of monosaccharides and biomass-derived carboxylic acids, oxidation of carbohydrates,[4,5] dehydroxylation of alcohols and polyols,[6,7] and thermal and photoelectrochemical production of hydrogen.[8−12] At a fundamental level, the bridging oxygen vacancy defects on a rutile $TiO_2(110)$ surface have proven to be an ideal model platform for the studies of catalytic reactions of reducible oxides where lattice oxygen directly takes part in the chemical transformations (Mars—van Krevelen type of reactions), such as dehydroxylation, that are critical in biomass processing.[1−3,9,13]

Due to a number of different functional groups present in biomass feedstock, its utilization is extremely complex and therefore hard to understand and optimize. As such, smaller molecules with prototypical functional groups are often used as surrogates to explore the mechanisms of catalytic deoxygenation reactions. In this context, the simplest polyols, such as ethylene glycol (EG), propylene glycols (PG), and glycerol, are often used as model probe molecules to understand the dehydroxylation,

* Address correspondence to
Roger.Rousseau@pnnl.gov,
Zdenek.Dohnalek@pnnl.gov.

Received for review September 21, 2013
and accepted October 17, 2013.

10.1021/nn404934q

hydrogenation, and oxidation reactions that take place in biomass processing.[14]

While on single-crystalline oxide surfaces the reactivity of simple diols remains largely unexplored, EG has been studied extensively on single-crystalline metal surfaces.[15−20] On Ag(110), EG adsorbs reversibly but dissociates on a partially oxidized surface *via* O−H bond scission, forming ethylenedioxy ($-OCH_2CH_2O-$) and water below room temperature.[16] The dissociated species undergo further decomposition *via* C−H bond cleavage, yielding glyoxal $(CHO)_2$ and H_2 at 380 K. On Mo(110), EG undergoes double C−O bond scission, forming ethylene gas at 350 K.[18] Using IR spectroscopy, two adsorption geometries (*i.e.*, monodentate ($-OCH_2CH_2OH$) and bidentate ($-OCH_2CH_2O-$)) have been reported.[18] Most recently, a different bond breaking sequence was observed on Pt(111) and Ni/Pt(111) model catalysts.[19] On Pt(111), dissociation proceeds initially *via* O−H bond cleavage with subsequent scission of the C−H and second O−H bonds, whereas on the Ni/Pt surface, both O−H bonds are cleaved prior to C−H scission. Similarly on Rh(111) and Rh(100), both O−H bonds are cleaved and the ethylenedioxy species then further decomposes to CO and H_2.[17,20]

In contrast with metal surfaces, the thermal chemistry of glycols on oxide surfaces is not well understood.[21−23] In early work, EG was studied on stoichiometric and partially reduced $TiO_2(110)$ using temperature-programmed desorption (TPD).[21] A stoichiometric surface was prepared by annealing the sample in an oxygen background pressure, and a reduced surface was created by electron beam irradiation. The observed products were EG, water, and ethylene. At higher temperatures, the main products were acetaldehyde, ethylene, and water with small amounts of ethanol and hydrogen also produced. Recently, we have also studied the coverage dependence of the reaction products from EG on a well-defined, partially reduced $TiO_2(110)$.[23] Ethylene and water were found to be the primary products for EG adsorbed both on bridging oxygen (O_b) vacancy (V_O) and 5-fold-coordinated Ti atoms (Ti_{5c}) sites at low EG coverages (<0.2 monolayer, ML). At higher EG coverages, a second reaction channel accounting for half of the reaction products, acetaldehyde and hydrogen, was also observed.

We have also employed scanning tunneling microscopy (STM) and density functional theory (DFT) to show that at very low coverages (<0.05 ML) 1,3-propylene glycol (1,3-PG) preferentially dissociates at V_O's at 300 K, forming nascent pairs of bridging hydroxy (HO_b) and hydropropoxy ($O_b(CH_2)_3OH$) species.[24] In these experiments we have also elucidated the rotational dynamics of the $O_b(CH_2)_3OH$ species and the dissociation dynamics of the second Ti_{5c}-bound OH group.

EG was studied in detail on $CeO_2(111)$ thin films.[22] On stoichiometric films, EG was found to dissociate *via* deprotonation of either one or both OH groups and form hydroxyethoxy/ethylenedioxy species and surface hydroxyls. After annealing, ethylenedioxy further decomposed into formate *via* C−C bond cleavage, ultimately yielding CO, CO_2, and H_2O products in TPD. On the reduced surface, ethylenedioxy dehydrated *via* C−O bond cleavage to form enolate ($OCHCH_2$), which ultimately yielded acetaldehyde, ethylene, and acetylene products.

In this study, we focus on following the complete sequence of elementary steps in the conversion of both EG and 1,3-PG with $TiO_2(110)$ at low coverages, and as a function of temperature, using a combination of STM, TPD, and DFT. The use of these two diol reactants allows us to compare and contrast the chemistries of two functionally similar molecules with different steric constraints, thereby allowing us to understand how molecular geometry may influence the observed chemical reactivity. Our temperature-dependent studies provide evidence for O−H dissociation of Ti_{5c}-bound diols at temperatures as low as 125 K and diol diffusion to and dissociation in V_O sites *via* both C−O and O−H bond cleavage above ~230 K; illustrate the dissociation dynamics of the second Ti_{5c}-bound OH group at 300 K; reveal the formation of a new high-temperature intermediate above ~400 K; and identify alkenes and water as the only products (at low coverages) released into the gas phase. These studies clearly demonstrate that the simple dehydration reactions expected for these diols on $TiO_2(110)$ proceed by an unexpectedly complex and rich series of reaction steps. These results provide an unprecedented level of quantitative, molecular-level detail on this hitherto poorly understood chemical reaction.

RESULTS AND DISCUSSION

Adsorption at Low Temperatures. Figure 1 shows a time-lapse sequence of STM images of the same area after $TiO_2(110)$ exposure to a small amount of EG at ~125 K. The corresponding ball models displayed beneath the STM images illustrate the observed processes along with the energy barrier values, ΔE, calculated using DFT. Typically, tunneling into empty states is employed to image $TiO_2(110)$.[1,3,13] In this mode, the rows of low-lying Ti_{5c} ions are imaged bright, whereas the rows of high-lying O_b ions are imaged dark, as seen in Figure 1. Further, the V_O defects (several labeled in Figure 1a) appear as faint protrusions on top of the dark O_b rows. A small amount of HO_b species is also generally observed as a result of water adsorption (from the chamber background) and dissociation on V_O's, $H_2O(g) + V_O + O_b \rightarrow 2HO_b$.[1,13]

Subsequent to the EG dose at 125 K, large bright protrusions appeared in the STM images on the Ti_{5c} rows. One such feature is shown in Figure 1a (labeled EG). Although the thermodynamically preferred adsorption sites are V_O's,[24] at low temperatures (<230 K), under

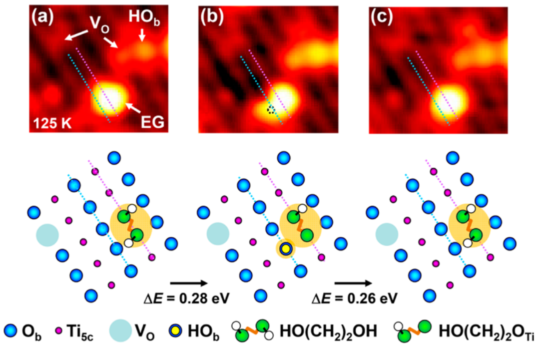

Figure 1. Time-lapse sequence of STM images of the same area on TiO$_2$(110) recorded 1 min apart after exposure to a small amount (∼0.01 ML) of ethylene glycol (EG) at ∼125 K. The cyan and magenta dotted lines illustrate the positions of O$_b$ and Ti$_{5c}$ rows. V$_O$, HO$_b$, and EG mark the positions of bridging oxygen vacancies, bridging hydroxyls, and ethylene glycol, respectively. Spacing of 6.5 Å between the bright Ti$_{5c}$ rows serves as a convenient scale in the images. Ball models below the images show the interpretation of the observed events. Yellow (white)-colored hydrogen atoms indicate that they are visible (invisible) in the STM. The energy barriers, ΔE, for the observed processes were determined using DFT (see text for further details). An additional example is provided in the Supporting Information (SI) as Figure S4.

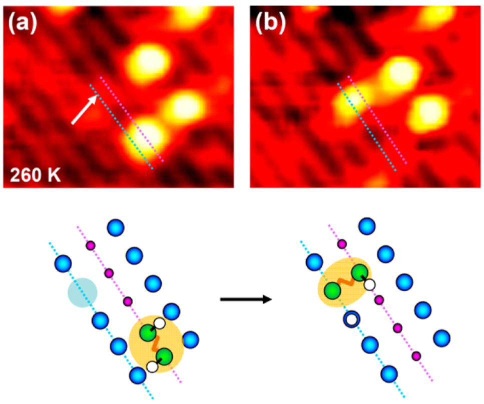

Figure 2. Time-lapse sequence of STM images of the same area on TiO$_2$(110) after exposure to EG at ∼260 K. See Figure 1 for the legend. An additional example is provided in the SI as Figure S5.

limited mobility conditions, the majority of EG molecules are found on Ti$_{5c}$ rows, indicating that the abundant Ti$_{5c}$ sites are the dominant initial adsorption sites. The sequence displayed in Figure 1 further shows that the Ti$_{5c}$-bound EG can easily dissociate *via* O−H bond cleavage, forming Ti$_{5c}$-bound hydroxyethoxy, HO-(CH$_2$)$_2$-O$_{Ti}$, and bridging hydroxyl, HO$_b$, *via* the following reaction:

$$\text{HO-(CH}_2)_2\text{-OH} + \text{O}_b \rightleftarrows \text{HO-(CH}_2)_2\text{-O}_{\text{Ti}} + \text{HO}_b \quad (1)$$

The STM of the observed HO-(CH$_2$)$_2$-O$_{Ti}$ + HO$_b$ pair is displayed in Figure 1b. In this image the originally symmetric EG molecule shows a new less bright feature on the lower left side of the original EG molecule. While the image in Figure 1b does not provide direct evidence for this particular reaction, prior studies (experimental and theoretical) of water,[25,26] alcohols,[27] and diols[24,28] convincingly demonstrated that the Ti$_{5c}$-bound O−H groups can easily dissociate *via* an acid/base reaction and hydrogen transfer to one of the neighboring O$_b$ sites.[13] DFT calculations for EG further support this picture, as the value of the calculated dissociation barrier is only 0.28 eV with the dissociated state being practically indentical in energy (higher by 0.02 eV). The energetically close-to-degenerate nature of the molecular and dissociated state is further demonstrated by the last image (Figure 1c), which shows the re-formation of the EG molecule. Finally, DFT simulations find essentially identical energetics for the protonation/deprotonation barriers for 1,3-PG, indicating that the OH groups of both diols are influenced by adsorption on the Ti$_{5c}$ by the same amount.

Dissociation in Bridging Oxygen Vacancies. To gain further insight into the dynamics of adsorbed species on Ti$_{5c}$ rows, additional experiments were carried out at temperatures that allow for slow EG diffusion that is observable by STM. The onset of EG diffusion along the Ti$_{5c}$ rows is observed at ∼230 K. Figure 2 shows a sequence of two STM images obtained at ∼260 K immediately after exposure to EG. Figure 2a exhibits three bright features due to EG molecules adsorbed on Ti$_{5c}$ rows. The EG (bottom, center) on the marked Ti$_{5c}$ row (dotted magenta line) is located adjacent to the O$_b$ row (dotted cyan line) containing a V$_O$ defect (white arrow). The subsequent STM image in Figure 2b shows that EG moved upward along the marked Ti$_{5c}$ row and reacted on the V$_O$ site. As demonstrated in our previous study of 1,3-PG on TiO$_2$(110) at 300 K,[24] this reaction leads to irreversible O−H bond cleavage and formation of geminate pairs of hydroxyalkoxy, O$_b$-(CH$_2$)$_n$-OH, and hydroxy, HO$_b$, species on the same O$_b$ row as shown in the ball model schematic for EG in Figure 2a. This reaction step can be summarized as follows:

$$\text{HO-(CH}_2)_2\text{-OH} + \text{V}_\text{O} + \text{O}_b \rightarrow \text{O}_b\text{-(CH}_2)_2\text{-OH} + \text{HO}_b \quad (2)$$

Due to the lower brightness, the HO$_b$ species cannot be observed next to the bright O$_b$-(CH$_2$)$_2$-OH, analogous to the case of HO$_b$ next to the alkoxy species formed by the dissociation of larger aliphatic alcohols as reported previously.[29,30] It should be noted that in contrast with the Ti$_{5c}$-bound EG molecule (Figure 2a), which is positioned on top of the Ti$_{5c}$ row, the O$_b$-(CH$_2$)$_2$-OH species is positioned between the Ti$_{5c}$ and O$_b$ rows. This is a consequence of strong binding of the second OH (in the O$_b$-(CH$_2$)$_2$-OH) on the Ti$_{5c}$ sites, as schematically shown in Figure 2b.

In addition to the dissociation of one EG, the image in Figure 2b also illustrates diffusion of the second EG (in the upper section of the image) downward by one lattice constant along the Ti$_{5c}$ row.

In our prior studies of alcohols[29−31] we have shown that the initial alcohol dissociation on V$_O$'s occurs *via* O−H bond cleavage. Consequently, the bright alkoxy

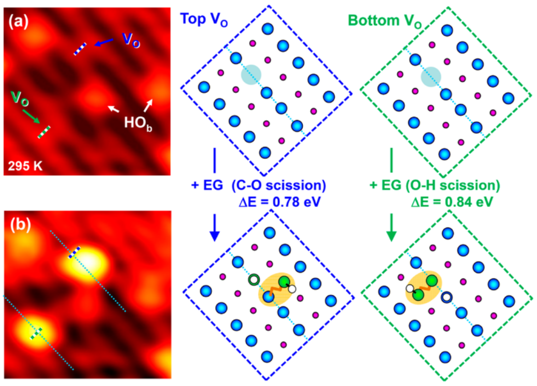

Figure 3. Room-temperature STM images of the same area on TiO_2(110) obtained (a) before and (b) after the exposure to EG at 295 K. The schematics on the right indicate the interpretation of the chemical processes observed in the images. The energy barriers, Δ*E*, for the C−O and O−H dissociation processes were determined using DFT. See Figure 1 for the legend.

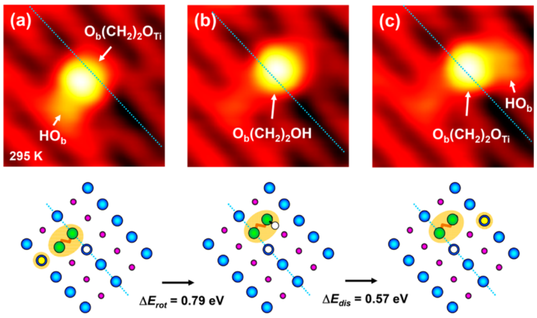

Figure 4. Time-lapse sequence of STM images of the same area on TiO_2(110) obtained after the exposure to EG at 295 K. The schematics below the images indicate the interpretation of the chemical processes observed in the images. The energy barriers for the O_b-$(CH_2)_2$-OH dissociation (ΔE_{dis}) and rotation (ΔE_{rot}) were determined using DFT (see text for further details). See Figure 1 for the legend. An additional example is provided in the SI as Figure S7.

species containing the O atom from the alcohol molecule always appeared in the position of the original V_O. Similarly, we have reported for 1,3-PG dissociation that the majority (90%) of bright O_b-$(CH_2)_3$-OH features also appear in the positions of the original V_O sites, revealing that the dissociation occurs predominantly *via* O−H cleavage as well.[24]

Surprisingly, the situation is significantly different for EG, where only 40% of the bright O_b-$(CH_2)_2$-OH species are located on top of the original V_O's. The remaining 60% appear on the neighboring O_b, as illustrated in Figure 3. Two O_b-$(CH_2)_2$-OH species are shown in Figure 3b following EG adsorption on clean TiO_2(110) (Figure 3a). While the bottom O_b-$(CH_2)_2$-OH (labeled green) is on top of the original V_O, the top O_b-$(CH_2)_2$-OH (blue) is displaced by one O_b along the O_b row. The interpretation presented in the blue schematics strongly suggests that on the blue V_O the EG molecule dissociated *via* C−O bond scission, forming the HO_b (not visible in the image) that contains the O atom from the molecule on top of the original V_O and the bright O_b-$(CH_2)_2$-OH displaced by one O_b. A closer comparison of the O−H bond (green) and C−O (blue) bond cleavage scenarios in the schematics reveals that the final surface intermediates (and the initial reactants) are the same for both cases, and therefore the reaction pathways are entirely controlled by the relative kinetic barriers for O−H and C−O bond scission. Our studies of alcohols and diols clearly show that the C−O scission is too high in energy to be accessed for alcohols, becomes a minority channel for 1,3-PG (∼10%) and majority channel for EG, indicating that the proximity of the second OH in the molecule is critical.

To gain further understanding of the underlying dissociation mechanisms, we turn to theoretical simulations. The dissociation barriers for O−H and C−O bond scission are determined by DFT to be 0.84 and 0.78 eV for EG and 0.74 and 0.98 eV for 1,3-PG, respectively. Both reactions lead to equivalent minima, which are lower in energy by 1.18 and 1.61 eV relative to EG and 1,3-PG chemisorbed on a Ti_{5c} row. These values are in agreement with the experimentally observed trends showing that for EG both C−O and O−H bond scission are kinetically similar, whereas for 1,3-PG O−H scission is expected to be the dominant pathway. Detailed analysis of the dissociation pathways shows that differences in the C−O scission for EG and 1,3-PG are primarily the result of geometric rather than electronic factors. While the longer 1,3-PG molecule can be bound with one OH group on the Ti_{5c} row and reach a V_O site with the other OH without inducing a significant strain, in the shorter EG, the C−O bond is being stretched and weakened as the V_O is reached. As a consequence, the barrier for C−O cleavage in EG is significantly lowered.

Room-Temperature Dynamics of O_b-$(CH_2)_n$-OH Species. In our previous room-temperature study of 1,3-PG we have shown that O_b-$(CH_2)_3$-OH exhibits a complex dynamics in terms of both the hindered rotational motion about its O_b anchor and the dissociation of its second Ti_{5c}-bound OH group.[24] The dynamics observed for O_b-$(CH_2)_2$-OH (formed by EG dissociation) are similar, and for completeness are summarized here in Figure 4.

The image in Figure 4a shows two features on two neighboring O_b rows, O_b-$(CH_2)_2$-O_{Ti} and HO_b. These features formed as a result of the dissociation of the Ti_{5c}-bound hydroxyl group of O_b-$(CH_2)_2$-OH species according to the following reaction:

$$O_b\text{-}(CH_2)_n\text{-}OH + O_b \rightleftarrows O_b\text{-}(CH_2)_n\text{-}O_{Ti} + HO_b \qquad (3)$$

This process is analogous to the OH dissociation of the Ti_{5c}-bound EG shown in Figure 1 and reaction 1. The DFT calculations show that the energy barriers for reaction 3 are 0.57 and 0.26 eV for O_b-$(CH_2)_2$-OH and O_b-$(CH_2)_3$-OH, respectively. The larger value for O_b-$(CH_2)_2$-OH is a consequence of the increased

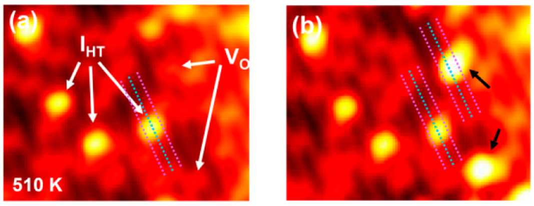

Figure 5. Room-temperature STM images of the same area on $TiO_2(110)$ obtained (a) after the exposure to EG at 295 K and 2 min annealing at 510 K and (b) after an additional dose of EG (~0.01 ML) at 295 K.

distance between the OH group and the O_b row where hydrogen is being transferred to. While the second hydrogen from the geminate HO_b is not seen in the STM images in Figure 4, it is likely positioned on one of the O_b's next to the O_b anchoring the O_b-$(CH_2)_2$-OH and/or O_b-$(CH_2)_2$-O_{Ti} species, as shown in the schematics of Figure 4.[24] Interestingly, in Figure 4b the HO_b disappears from the neighboring O_b row, indicating reformation of O_b-$(CH_2)_2$-OH species and demonstrating the dynamic equilibrium indicated in reaction 3. This event is subsequently followed by another dissociation process on a different O_b row, as illustrated in Figure 4c. The complete reaction sequence containing additional events was recorded as an STM movie, which is provided in the SI as Figure S6.

In addition to the dissociation of O_b-$(CH_2)_2$-OH species, the images in Figure 4a and b also illustrate the rotation of the HO-$(CH_2)_2$-O_b about the anchoring O_b site. In this process the alkyl chain with the Ti_{5c}-bound OH group rotates between the two equivalent Ti_{5c} rows that are neighboring the anchoring O_b row (dotted cyan line in Figure 4). The theoretically determined values for the rotational barriers for O_b-$(CH_2)_2$-OH and O_b-$(CH_2)_3$-OH are 0.79 and 0.95 eV. The lower rotational barrier for the O_b-$(CH_2)_2$-OH species is caused by a shorter chain length, which allows only for the formation of a weaker bond between the OH oxygen and Ti_{5c} site. The DFT studies further show that the cross-row rotations of O_b-$(CH_2)_2$-O_{Ti} and O_b-$(CH_2)_3$-O_{Ti} are much higher in energy, with barriers on the order of 2.5 eV in both cases.

High-Temperature Intermediate. To further understand the transformations that the O_b-$(CH_2)_n$—OH and O_b-$(CH_2)_n$-O_{Ti} intermediates undergo at higher temperatures (>400 K), we have carried room temperature imaging following the annealing to elevated temperatures as well as a direct high temperature imaging during the dose.

The results of the imaging after annealing the preadsorbed EG at 510 K are shown in Figure 5a. The image shows three bright features marked as high-temperature intermediate, I_{HT}. The appearance of the I_{HT} in the images is significantly different from the O_b-$(CH_2)_2$-OH and O_b-$(CH_2)_2$-O_{Ti} species that are observed directly after adsorption between 230 and 300 K. While the O_b-$(CH_2)_2$-OH and O_b-$(CH_2)_2$-O_{Ti} species are centered between the O_b and Ti_{5c} row (see Figures 3 and 4), the I_{HT}'s are centered on top of the O_b row. This can be clearly seen on the feature that is overlaid with the position of the O_b (cyan dotted line) and neighboring Ti_{5c} (magenta) rows.

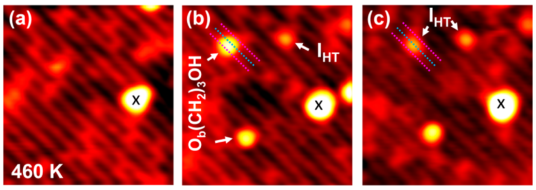

Figure 6. Time-lapse sequence of STM images of the same area on $TiO_2(110)$ obtained at 460 K: (a) clean surface, (b) surface after 1,3-PG adsorption, and (c) after an additional 6 min of scanning. The large feature (possibly a TiO_x cluster) labeled with × was used to track the same area at high temperatures. An additional example is provided in the SI as Figure S9.

To further evaluate the differences in the appearance of I_{HT} and O_b-$(CH_2)_2$-OH/O_b-$(CH_2)_2$-O_{Ti} features, we have imaged the same area after an additional EG dose at 295 K. Two new O_b-$(CH_2)_2$-OH features appear in Figure 5b (marked by black arrows) as a result of EG dissociation in the V_O's (labeled in Figure 5a). The direct comparison in the same image further demonstrates that the O_b-$(CH_2)_2$-OH species are brighter and larger in size.

Similar conclusions to those presented above can be drawn based on the direct high-temperature imaging during 1,3-PG dosing at 460 K (Figure 6). A time-lapse video from the same area is provided in the SI as Figure S8. Three images presented in Figure 6 illustrate the dissociation of 1,3-PG on V_O's (Figure 6b) with subsequent conversion of the O_b-$(CH_2)_3$-OH/O_b-$(CH_2)_3$-O_{Ti} species to the I_{HT} intermediate (Figure 6c). In addition to the I_{HT} formation, the high-temperature imaging also shows that O_b-$(CH_2)_3$-OH/O_b-$(CH_2)_3$-O_{Ti} and I_{HT} species do not diffuse at 460 K. The facile motion of V_O's (as well as HO_b hydrogen) can be seen in the time-lapse video (Figures S8), in agreement with our previous quantitative studies of their diffusion.[32,33]

The time-lapse video also shows a lack of rotational motion for extended periods of time, indicating that the observed species are mostly in the form of O_b-$(CH_2)_3$-O_{Ti} and not O_b-$(CH_2)_3$-OH species. This is not surprising considering the ease of O_b-$(CH_2)_3$-OH dissociation according to reaction 3 demonstrated at lower temperatures (230—295 K) and the high mobility of the HO_b hydrogen, allowing for its spatial separation from the O_b-$(CH_2)_3$-O_{Ti} species. Occasional cross-O_b row rotation is observed as a result of the O_b-$(CH_2)_3$-O_{Ti} reaction with fast moving HO_b hydrogen, leading to rotationally active O_b-$(CH_2)_3$-OH species.

While the experiments do not allow us to determine the chemical identity of the I_{HT} species, they clearly indicate their high stability and long lifetime. Using the observations presented here and our prior studies

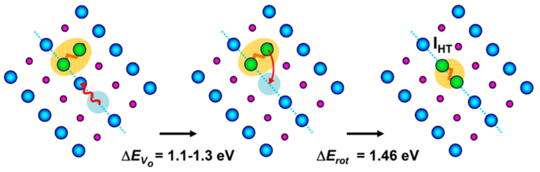

Figure 7. Proposed identity and mechanism of the formation for the I_{HT} intermediate. The energy barriers for V_O diffusion (ΔE_{V_O}) and O_b-$(CH_2)_2$-O_{Ti} rotation (ΔE_{rot}) were determined using DFT (see text for further details). See Figure 1 for the legend.

of V_O diffusion[32] as well as V_O-assisted alkoxy diffusion,[34] we propose that the formation of I_{HT} is assisted by V_O's as illustrated in Figure 7. In the proposed mechanism, the first step is V_O diffusion toward the O_b-$(CH_2)_2$-O_{Ti} species (Figure 7a). We have determined previously (both experimentally and theoretically) that the barrier for V_O diffusion along the O_b row is 1.1−1.3 eV, allowing for fast diffusion above ~400 K. This can be clearly observed in the time-lapse video in Figure S8.

The second step in the mechanism is the rotation of the Ti_{5c}-bound dioxo group about the O_b anchor into the empty O_b site created by the diffusing V_O, as schematically shown in Figure 7b. This results in the formation of a new dioxo intermediate that is bound to two neighboring O_b sites (Figure 7c). This process can be summarized by the following reaction:

$$O_b\text{-}(CH_2)_n\text{-}O_{Ti} + V_O \rightarrow O_b\text{-}(CH_2)_n\text{-}O_b \qquad (4a)$$

Alternatively, the O_b-$(CH_2)_n$-O_{Ti} intermediate can react with a diffusing hydrogen atom to form O_b-$(CH_2)_n$-OH according to reverse reaction 3, and the O_b-$(CH_2)_n$−OH species can subsequently rotate and fill the neighboring V_O:

$$O_b\text{-}(CH_2)_n\text{-}OH + V_O + O_b \rightarrow O_b\text{-}(CH_2)_n\text{-}O_b + HO_b \qquad (4b)$$

The energetics of the reaction pathways summarized in reactions 4a and 4b were further studied *via* DFT. The V_O migration toward the bound glycol was found to have activation energy barriers of 1.1−1.3 eV (depending on where the excess electrons associated with the V_O site were located), in accord with our previous studies.[32,34] The activation energy barriers for O_b-$(CH_2)_2$-O_{Ti} and O_b-$(CH_2)_2$-OH rotation into the neighboring V_O were found to be 1.46 and 0.52 eV, respectively. Analogously, for O_b-$(CH_2)_3$-O_{Ti} and O_b-$(CH_2)_3$-OH the barriers are 1.18 and 0.68 eV, respectively, indicating that all these processes can indeed be facile around 500 K.

It should be noted that while the barriers for the reaction of oxohydroxo species, O_b-$(CH_2)_n$-OH, into V_O are very low, the reaction is in fact a three-body process (O_b-$(CH_2)_2$-O_{Ti} + V_O + HO_b), and as such, the rates for this reaction will be fairly low.

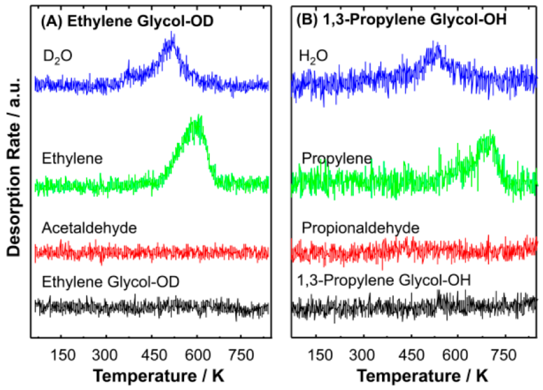

Figure 8. TPD spectra of the desorbing species observed following the 0.05 ML dose of (A) ethylene glycol−OD and (B) propylene glycol−OH at 90 K. The desorption of EG-OD was monitored at 32 amu, which is the most intense cracking fragment. Desorption of D_2O at 20 amu, ethylene (CH_2CH_2) at 27 amu, and acetaldehyde (CH_3CHO) at 29 amu.[23] The desorption of 1,3-PG-OH was monitored at 31 amu, which is the most intense cracking fragment. Desorption of H_2O at 18 amu, propylene (CH_2CHCH_3) at 41 amu, and propionaldehyde (CH_3CH_2CHO) at 58 amu.

Gas Phase Products. The final step in the conversion of EG[23] and 1,3-PG at low coverages is the formation and liberation of gas phase products from the O_b-$(CH_2)_n$-O_b species. To follow the product desorption, we employed TPD. As shown in Figure 8, the only products observed for coverages that correspond to saturation of V_O's by EG and/or 1,3-PG are water and ethylene and/or water and propylene, respectively. Water is the first product observed between 450 and 550 K. This temperature range is below the alkene evolution temperature and is the same as the temperature for the recombinative desorption of H_2O from two HO_b species, $2HO_b \rightarrow H_2O(g) + V_O$.[35,36] The origin of hydrogen atoms in water that formed is further revealed by experiments with deuterium-labeled hydroxyl groups in EG, DO-$(CH_2)_2$-OD, as shown in Figure 8a. The experiments clearly show only D_2O formation (not H_2O), which demonstrates that hydrogen originates from the cleavage of the glycol hydroxyl groups and not CH groups. This is also supported by our STM observation of the EG and 1,3-PG OH group dissociation and HO_b formation at lower temperatures presented in Figures 1−4.

The only observed carbon-containing products are ethylene and propylene from EG and 1,3-PG, respectively. While ethylene desorption peaks at ~600 K (Figure 8a), propylene is observed at ~700 K (Figure 8b).

Theoretically, we first describe the simpler results for the product formation from EG. We observe that the desorption of ethylene from the O_b-bound dioxo, O_b-$(CH_2)_2$-O_b, species has an extremely high barrier (>4.0 eV) when both C−O bounds are broken simultaneously. This is in accord with the fact that this process is essentially a 2+2 cycloaddition and is symmetry forbidden based on Woodward−Hoffmann rules.[37]

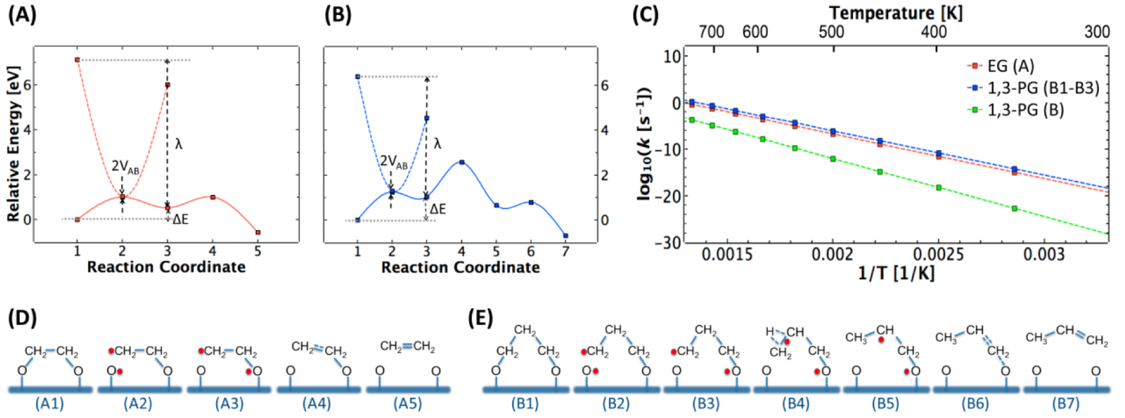

Figure 9. Desorption energy profile of EG (A) and 1,3-PG (B) including an excited state potential energy surface for the first step. The desorption rates shown in (C) include nonadiabatic coupling for EG (blue) and 1,3-PG (red) along with the overall desorption rate of 1,3-PG (green) obtained from TST. Parameters from Marcus theory used to estimate the rates of electron transfer processes (indicated in the figure) are estimated by charge-constrained DFT simulations (see SI for further discussion). Schematics illustrating desorption mechanisms for EG and 1,3-PG are shown in (D) and (E).

On the other hand, sequential homolytic cleavage of C$-$O bonds exhibits a barrier on the order of only 1.0 eV, as shown in Figure 9A. On the basis of a transition state theory (TST) estimate of the reaction rate, this energy barrier would yield a desorption temperature of ~360 K, which is appreciably lower than ~600 K observed experimentally. This discrepancy can be resolved by noting that the first C$-$O$_b$ bond scission results in unpaired electron density on the O$_b$ (Figure 9D, panel A2), which would correspond to a localized radical state or hole state. In order to facilitate the second CO bond cleavage event, the hole state needs to migrate to the adjacent O$_b$ site *via* a charge transfer event (A2 → A3), which shifts the localized unpaired electron density onto the O$_b$ site where the second (as yet undissociated) C$-$O$_b$ bond resides. As noted previously,[38] the hole migration processes of this geometrical arrangement in rutile TiO_2 are nonadiabatic in nature and thus are kinetically hindering. Indeed this observation is supported by the current calculations, which find a close lying excited state (*i.e.*, within 0.1 eV) at the transition state of the first CO bond cleavage event, which would also imply a strong nonadiabatic component to the reaction kinetics.[39]

These observations lead us to propose a coupled C$-$O bond breaking/electron transfer reaction as one of the steps in the formation of both ethylene and propylene. As described, ethylene desorption mechanistically occurs by two sequential C$-$O bond breaking steps where only the first one exhibits a small separation between the ground and excited state at the transition state and hence is anticipated to have a large nonadiabatic component to the reaction rate.

To evaluate the kinetic parameters for the proposed mechanism (Figure 9D), we employed Marcus theory for describing the nonadiabatic charge transfer steps and TST for the adiabatic steps (see SI for further discussion). For the first C$-$O bond breaking step, two different adiabatic pathways can be defined by monitoring the position of the resulting radical electron on O$_b$ sites yielding two adiabatic surfaces as illustrated in Figure 9A. The nonadiabatic reaction rate for the electron transfer estimated from Marcus theory is shown in Figure 9C (red). The determination of the required parameters, namely, the reaction energy, ΔE; reorganization energy, λ (calculated from constrained DFT); and electron coupling, V_{AB} (calculated from both constrained DFT and time-dependent density functional theory with the time-dependent fast Fourier transform), is described in the SI. Generally, typical values of the rate constants in TPD at the peak desorption temperature are on the order of 0.1 ML/s. Factoring in the nonadiabatic effects on the reaction kinetics, the rate constant for EG (Figure 9C, red) reaches 0.1 ML/s at ~700 K in reasonable agreement with the experiment.

For 1,3-PG, the overall mechanism is slightly more complex (Figure 9B and E) compared to EG, as it involves an additional H transfer step (Figure 9E, B3 → B5). The initial steps (B1 → B3), which include the first C$-$O bond cleavage and e$^-$ transfer, are identical with that for EG and yield a similar rate constant (Figure 9C, blue). We note, however, that the H transfer step represents an overall rate-limiting step (distinct from EG) hindered by an additional 1.5 eV barrier that has to be surmounted before propylene desorption. Using TST we estimate that the rate constant from this sequential C$-$O bond breaking and H -transfer process (Figure 9C, green) is on the order of 0.1 ML/s around 750$-$800 K. A higher desorption temperature as compared to ethylene is in agreement with our TPD measurements, where EG is observed at 600 K and PG at 700 K.

CONCLUSIONS

In summary, our study provides the first examination of diol dehydration on metal oxide surfaces with a detailed quantitative mechanistic evaluation of the individual underlying molecular-level steps. In contrast to alcohols, where previous work has shown a simple concerted heterolytic C−O bond breaking/β-H proton transfer step to produce alkenes,[40,41] the formation of alkenes from diols proceeds *via* a relatively complex series of correlated reaction steps. We show that Ti_{5c} site bound O−H groups of both molecularly adsorbed glycols and dissociated oxohydroxo intermediates can easily dissociate and re-form, thus forming a dynamic equilibrium. The irreversible dissociation of molecularly bound glycols that occurs in bridging oxygen vacancies is found to proceed *via* two competitive channels involving C−O and/or O−H bond scission. The comparison of EG and 1,3-PG yields a molecular-level understanding of how steric effects introduced by the second, Ti_{5c}-bound OH can weaken the C−O bond and thereby facilitate its cleavage. At elevated temperatures (>400 K), formation of a new intermediate is observed and interpreted to be a result of the reaction of diffusing V_O with the Ti_{5c}-bound oxygen of the dioxo/oxohydroxo species. The final step, the formation of alkenes, as the only C-containing gas phase products is found to proceed *via* sequential homolytic C−O bond cleavage accompanied by nonadiabatic electron transfer. As such, the observed behavior points to an extremely rich and heretofore unanticipated chemistry of glycols on oxides.

METHODS

Experimental Details. The experiments were performed in two separate ultrahigh-vacuum (UHV) systems: (1) a scanning tunneling microscopy system for spatially resolved imaging and (2) a molecular beam system for TPD studies. The systems are briefly described below.

The STM experiments were carried out in a UHV chamber (base pressure $\leq 1 \times 10^{-10}$ Torr) equipped with an Omicron variable-temperature STM. Well-ordered, partially reduced rutile $TiO_2(110)$-(1×1) surfaces were prepared by repeated cycles of Ne^+ sputtering and 900 K annealing of the single-crystalline TiO_2 sample (10 × 2 × 0.5 mm^3, Princeton Scientific). The surface order and cleanliness were checked using low-energy electron diffraction (LEED) and Auger electron spectroscopy (AES). Electrochemically etched and UHV-annealed tungsten tips were used for imaging. All STM images were recorded in constant-current mode at a positive sample bias of 1.2−1.6 V and tunneling currents of 5−80 pA and processed using WSxM software (Nanotech, freeware).[42] The concentration of V_O's on the samples ranged from 0.03 to 0.09 monolayer. Ethylene glycol (Sigma-Aldrich, ≥ 99.8%) and 1,3-propylene glycol (Sigma-Aldrich, ≥ 97%) were purified by several freeze−pump−thaw cycles using liquid nitrogen and dosed on $TiO_2(110)$ in the STM stage *via* a retractable tube doser. In all STM experiments, the EG coverage was kept very low (~0.01 ML) to keep the observed molecules isolated.

The TPD experiments were conducted in a UHV molecular beam surface scattering apparatus (base pressure $<1 \times 10^{-10}$ Torr) equipped with AES, LEED, X-ray photoelectron spectroscopy (XPS), a quartz crystal microbalance (QCM, XTM/2-Inficon), and a quadrupole mass spectrometer (QMS, UTI-100C) for TPD studies. The rutile $TiO_2(110)$-1×1 crystal (10 × 10 × 1 mm^3, Princeton Scientific) was bonded with ceramic glue (Aremco Ultra-Temp 516) onto a Ta plate as described in our earlier publication.[43] The temperature (70−900 K) was measured using a thermocouple glued to the edge of the crystal. The TPD spectra (90−800 K, 1.0 K/s) were taken with the crystal in a line-of-sight geometry with the QMS. The initial surface cleaning procedure comprised cycles of Ne^+ sputtering (1.5 kV, 10 μA) at 300 K and subsequent annealing at 850−900 K for 5−10 min until a clean and ordered $TiO_2(110)$-1×1 surface was obtained based on AES, XPS, and LEED. To maintain the clean surface, a brief, 3 min sputtering at 300 K followed by 5 min of annealing at 850 K was used on a daily basis. Reproducibility of the surface structure was further confirmed using the H_2O TPD line shape.[44] The V_O concentration of ~5% was determined based on the ratio of water recombination desorption peak area at ~500 K to the monolayer desorption peak at 284 K.[44,45] Ethylene glycols (ethylene glycol 99.8%, ethylene glycol-$(OD)_2$, ethylene-D_4 glycol 98%) and 1,3-propylene glycol (≥97%) were obtained from Sigma-Aldrich and transferred into round-bottom flasks with baked molecular sieves (to remove water). Before introducing into the chamber, the diols were pumped at room temperature to further minimize the effect of water and then stabilized in a water bath (318 K) for ~2 h. The gas lines were heated to avoid the condensation of the molecules. The molecules were dosed onto the substrate using an effusive molecular beam; the fluxes of the molecules were constant as measured by a QCM and determined by the TPD experiment, allowing us to precisely control the dose.[45]

Computational Details. Calculations were carried out employing DFT with a gradient-corrected functional for exchange and correlation[46] as implemented in the CP2K package.[47,48] Core electrons are modeled as norm-conserving pseudopotentials.[49] The wave functions were expanded in a molecularly optimized double-ζ Gaussian basis set to minimize basis set superposition errors.[50] An additional auxiliary plane wave basis of 300 Ry energy cutoff was used for the calculation of the electrostatic energy terms. Dispersion forces, typically not well modeled by gradient-corrected functionals, are included by the DFT-D method of Grimme,[51] which we have shown previously to provide a good description for the conformational structure and dynamics for alkyl chains of octoxy species on $TiO_2(110)$.[30] All surface reactions were modeled on a (6×3) rutile-$TiO_2(110)$ surface slab of 4 TiO_2 trilayers' depth and a 12 Å thick vacuum layer to minimize electrostatic interactions between periodic images in the direction of the surface normal. Finally, the Γ-point approximation was employed for Brillouin zone integration. The energies of selected reaction steps were checked for convergence with respect to TiO_2 slab thickness and DFT-D description and were found to be converged within 0.1 eV. For an accurate description of excess electrons associated with the V_O, DFT+U theory[52] is used with effective $U = 4.1$ eV applied to the Ti 3d electrons within a local spin density approximation. This value of U is adopted, as it was found to adequately reproduce the work function, $W = 4.9$ eV,[53] and location of defect states at 0.8 eV below the conduction band.[54] See extended discussion of the choice of U parameter included in the SI.

Calculation of all reaction coordinates was performed using the climbing image nudged-elastic-band method (CI-NEB)[55,56] employing 12 replicas. Minimization of our CI-NEB was performed by *ab initio* molecular dynamics, where each replica of the NEB is given an initial temperature of 500 K and annealed to 0 K over a time scale of 1−2 ps, leading to a residual maximum component to the forces on the atoms of less than 1×10^{-3} atomic units. This approach allows us to explore the nearby configurations in phase space to obtain a path that may be substantially different (and lower in energy) than our initial conditions but does not guarantee that we have the absolute lowest energy path connecting two intermediates.

For the consideration of the impact of the nonadiabatic dynamics associated with the charge transfer processes we employ a Marcus theory[39,57,58] description for the estimation of reaction rate constants. Within this theory, the reaction rate includes nonadiabatic coupling charge transfer processes such as found for the first C−O bond scission leading to the formation of ethylene and propylene. Within this approach, the reaction rate can be obtained by the formula

$$k = \frac{2\pi}{\hbar}\,|V_{AB}|\,\frac{1}{\sqrt{4\pi\lambda k_B T}}\exp\left[\frac{-(\Delta E+\lambda)^2}{4\lambda k_B T}\right]$$

where V_{AB} is the electronic coupling, ΔE is the energy difference of two states, and λ is the reorganization energy. In order to obtain these parameters introduced in the Marcus formula, time-dependent density functional theory (TDDFT)[59,60] with the time-dependent fast Fourier transform (TDFFT) and constraint DFT (cDFT)[61,62] calculations are performed. A detailed discussion of the performance of the two approaches is given in the SI.

Conflict of Interest: The authors declare no competing financial interest.

Acknowledgment. X.L. is grateful for the support of the Linus Pauling Distinguished Postdoctoral Fellowship Program funded by Laboratory Directed Research and Development Program at Pacific Northwest National Laboratory (PNNL). Z.Z. acknowledges the American Chemical Society Petroleum Research Fund for the support of this research. Other authors were supported by the U.S. Department of Energy, Office of Basic Energy Sciences, Division of Chemical Sciences, Geosciences & Biosciences, and the work was performed in EMSL, a national scientific user facility sponsored by the Department of Energy's Office of Biological and Environmental Research and located at Pacific Northwest National Laboratory (PNNL). PNNL is a multiprogram national laboratory operated for the DOE by Battelle.

Supporting Information Available: Selection of *U* parameter used in DFT+U calculations; determination of desorption parameters from nonadiabatic Marcus theory; STM movies illustrating the dissociation and rotation of the O_b-$(CH_2)_2$-OH species and formation of the high-temperature O_b-$(CH_2)_2$-O_b intermediate; additional examples of processes illustrated in Figures 1, 2, 4, and 6; Cartesian coordinates of all intermediates and transitions states obtained *via* DFT. This material is available free of charge *via* the Internet at http://pubs.acs.org.

REFERENCES AND NOTES

1. Diebold, U. The Surface Science of Titanium Dioxide. *Surf. Sci. Rep.* **2003**, *48*, 53–229.
2. Henderson, M. A. A Surface Science Perspective on TiO_2 Photocatalysis. *Surf. Sci. Rep.* **2011**, *66*, 185–297.
3. Pang, C. L.; Lindsay, R.; Thornton, G. Structure of Clean and Adsorbate-Covered Single-Crystal Rutile TiO_2 Surfaces. *Chem. Rev.* **2013**, *113*, 3887–3948.
4. Besson, M.; Gallezot, P.; Pinel, C. Conversion of Biomass into Chemicals over Metal Catalysts. *Chem. Rev.* **2013**, *10*, 1021/cr4002269.
5. Davis, S. E.; Ide, M. S.; Davis, R. J. Selective Oxidation of Alcohols and Aldehydes over Supported Metal Nanoparticles. *Green Chem.* **2013**, *15*, 17–45.
6. ten Dam, J.; Hanefeld, U. Renewable Chemicals: Dehydroxylation of Glycerol and Polyols. *ChemSusChem* **2011**, *4*, 1017–1034.
7. Katryniok, B.; Paul, S.; Dumeignil, F. Recent Developments in the Field of Catalytic Dehydration of Glycerol to Acrolein. *ACS Catal.* **2013**, *3*, 1819–1834.
8. Liu, C. J.; Burghaus, U.; Besenbacher, F.; Wang, Z. L. Preparation and Characterization of Nanomaterials for Sustainable Energy Production. *ACS Nano* **2010**, *4*, 5517–5526.
9. Connelly, K. A.; Idriss, H. The Photoreaction of TiO_2 and Au/TiO_2 Single Crystal and Powder Surfaces with Organic Adsorbates. Emphasis on Hydrogen Production from Renewables. *Green Chem.* **2012**, *14*, 260–280.
10. Hambourger, M.; Kodis, G.; Vaughn, M. D.; Moore, G. F.; Gust, D.; Moore, A. L.; Moore, T. A. Solar Energy Conversion in a Photoelectrochemical Biofuel Cell. *Dalton Trans.* **2009**, 9979–9989.
11. Tanaka, A.; Sakaguchi, S.; Hashimoto, K.; Kominami, H. Preparation of Au/TiO_2 with Metal Cocatalysts Exhibiting Strong Surface Plasmon Resonance Effective for Photoinduced Hydrogen Formation under Irradiation of Visible Light. *ACS Catal.* **2012**, *3*, 79–85.
12. Alonso, D. M.; Bond, J. Q.; Dumesic, J. A. Catalytic Conversion of Biomass to Biofuels. *Green Chem.* **2010**, *12*, 1493–1513.
13. Dohnalek, Z.; Lyubinetsky, I.; Rousseau, R. Thermally-Driven Processes on Rutile TiO_2(110)-(1 × 1): A Direct View at the Atomic Scale. *Prog. Surf. Sci.* **2010**, *85*, 161–205.
14. Corma, A.; Iborra, S.; Velty, A. Chemical Routes for the Transformation of Biomass into Chemicals. *Chem. Rev.* **2007**, *107*, 2411–2502.
15. Bowker, M.; Madix, R. J. XPS, UPS and Thermal-Desorption Studies of Alcohol Adsorption on Cu(110): 2. Higher Alcohols. *Surf. Sci.* **1982**, *116*, 549–572.
16. Capote, A. J.; Madix, R. J. O-H and C-H Bond Activation in Ethylene-Glycol by Atomic Oxygen on Ag(110) - Heterometallacycle Formation and Selective Dehydrogenation to Glyoxal. *J. Am. Chem. Soc.* **1989**, *111*, 3570–3577.
17. Brown, N. F.; Barteau, M. A. Carbon-Halogen Bond Scission and Rearrangement of Beta-Halohydrins on the Rh(111) Surface. *J. Phys. Chem.* **1994**, *98*, 12737–12745.
18. Queeney, K. T.; Arumainayagam, C. R.; Weldon, M. K.; Friend, C. M.; Blumberg, M. Q. Differential Reactivity and Structure of Mono- and Dialkoxides: The Reactions of Ethylene Glycol on Mo(110). *J. Am. Chem. Soc.* **1996**, *118*, 3896–3904.
19. Salciccioli, M.; Yu, W. T.; Barteau, M. A.; Chen, J. G. G.; Vlachos, D. G. Differentiation of O-H and C-H Bond Scission Mechanisms of Ethylene Glycol on Pt and Ni/Pt Using Theory and Isotopic Labeling Experiments. *J. Am. Chem. Soc.* **2011**, *133*, 7996–8004.
20. Jansen, M. M. M.; Nieuwenhuys, B. E.; Niemantsverdriet, H. Chemistry of Ethylene Glycol on a Rh(100) Single-Crystal Surface. *ChemSusChem* **2009**, *2*, 883–886.
21. Farfan-Arribas, E.; Madix, R. J. Role of Defects in the Adsorption of Aliphatic Alcohols on the TiO_2(110) Surface. *J. Phys. Chem. B* **2002**, *106*, 10680–10692.
22. Chen, T. L.; Mullins, D. R. Ethylene Glycol Adsorption and Reaction over CeO_x(111) Thin Films. *J. Phys. Chem. C* **2011**, *115*, 13725–13733.
23. Li, Z.; Kay, B. D.; Dohnalek, Z. Dehydration and Dehydrogenation of Ethylene Glycol on Rutile TiO_2(110). *Phys. Chem. Chem. Phys.* **2013**, *15*, 12180–12186.
24. Zhang, Z. R.; Yoon, Y.; Lin, X.; Acharya, D.; Kay, B. D.; Rousseau, R.; Dohnalek, Z. OH Group Dynamics of 1,3-Propanediol on TiO_2(110). *J. Phys. Chem. Lett.* **2012**, *3*, 3257–3263.
25. Wendt, S.; Matthiesen, J.; Schaub, R.; Vestergaard, E. K.; Laegsgaard, E.; Besenbacher, F.; Hammer, B. Formation and Splitting of Paired Hydroxyl Groups on Reduced TiO_2(110). *Phys. Rev. Lett.* **2006**, *96*, 066107.
26. Du, Y.; Deskins, N. A.; Zhang, Z.; Dohnálek, Z.; Dupuis, M.; Lyubinetsky, I. Two Pathways for Water Interaction with Oxygen Adatoms on TiO_2(110). *Phys. Rev. Lett.* **2009**, *102*, 096102.
27. Hansen, J. O.; Huo, P.; Martinez, U.; Lira, E.; Wei, Y. Y.; Streber, R.; Laegsgaard, E.; Hammer, B.; Wendt, S.; Besenbacher, F. Direct Evidence for Ethanol Dissociation on Rutile TiO_2(110). *Phys. Rev. Lett.* **2011**, *107*, 136102.
28. Li, S. C.; Chu, L. N.; Gong, X. Q.; Diebold, U. Hydrogen Bonding Controls the Dynamics of Catechol Adsorbed on a TiO_2(110). *Surf. Sci.* **2010**, *328*, 882–884.
29. Zhang, Z.; Bondarchuk, O.; Kay, B. D.; White, J. M.; Dohnálek, Z. Direct Visualization of 2-Butanol Adsorption and Dissociation on TiO_2(110). *J. Phys. Chem. C* **2007**, *111*, 3021–3027.
30. Zhang, Z.; Rousseau, R.; Gong, J.; Kay, B. D.; Dohnálek, Z. Imaging Hindered Rotations of Alkoxy Species on TiO_2(110). *J. Am. Chem. Soc.* **2009**, *131*, 17926–17932.
31. Zhang, Z.; Bondarchuk, O.; White, J. M.; Kay, B. D.; Dohnálek, Z. Imaging Adsorbate O-H Bond Cleavage: Methanol on TiO_2(110). *J. Am. Chem. Soc.* **2006**, *128*, 4198–4199.

32. Zhang, Z.; Ge, Q.; Li, S. C.; Kay, B. D.; White, J. M.; Dohnálek, Z. Imaging Intrinsic Diffusion of Bridge-Bonded Oxygen Vacancies on TiO_2(110). *Phys. Rev. Lett.* **2007**, *99*, 126105.
33. Li, S. C.; Zhang, Z.; Sheppard, D.; Kay, B. D.; White, J. M.; Du, Y.; Lyubinetsky, I.; Henkelman, G.; Dohnálek, Z. Intrinsic Diffusion of Hydrogen on Rutile TiO_2(110). *J. Am. Chem. Soc.* **2008**, *130*, 9080–9088.
34. Zhang, Z. R.; Rousseau, R.; Gong, J. L.; Li, S. C.; Kay, B. D.; Ge, Q. F.; Dohnálek, Z. Vacancy-Assisted Diffusion of Alkoxy Species on Rutile TiO_2(110). *Phys. Rev. Lett.* **2008**, *101*, 156103.
35. Henderson, M. A. Structural Sensitivity in the Dissociation of Water on TiO_2 Single-Crystal Surfaces. *Langmuir* **1996**, *12*, 5093–5098.
36. Henderson, M. A. An HREELS and TPD Study of Water on TiO_2(110): The Extent of Molecular *versus* Dissociative Adsorption. *Surf. Sci.* **1996**, *355*, 151–166.
37. Woodward, R. B.; Hoffmann, R. The Conservation of Orbital Symmetry. *Angew. Chem., Int. Ed.* **1969**, *8*, 781–853.
38. Deskins, N. A.; Dupuis, M. Intrinsic Hole Migration Rates in TiO_2 from Density Functional Theory. *J. Phys. Chem. C* **2009**, *113*, 346–358.
39. Shin, S.; Metiu, H. Nonadiabatic Effects on the Charge-Transfer Rate-Constant - A Numerical Study of a Simple-Model System. *J. Chem. Phys.* **1995**, *102*, 9285–9295.
40. Kim, Y. K.; Kay, B. D.; White, J. M.; Dohnálek, Z. Inductive Effect of Alkyl Chains on Alcohol Dehydration at Bridge-Bonded Oxygen Vacancies of TiO_2(110). *Catal. Lett.* **2007**, *119*, 1–4.
41. Kim, Y. K.; Kay, B. D.; White, J. M.; Dohnálek, Z. Alcohol Chemistry on Rutile TiO_2(110): The Influence of Alkyl Substituents on Reactivity and Selectivity. *J. Phys. Chem. C* **2007**, *111*, 18236–18242.
42. Horcas, I.; Fernandez, R.; Gomez-Rodriguez, J. M.; Colchero, J.; Gomez-Herrero, J.; Baro, A. M. WSXM: A Software for Scanning Probe Microscopy and a Tool for Nanotechnology. *Rev. Sci. Instrum.* **2007**, *78*, 013705.
43. Bondarchuk, O.; Kim, Y. K.; White, J. M.; Kim, J.; Kay, B. D.; Dohnálek, Z. Surface Chemistry of 2-Propanol on TiO_2(110): Low- and High-Temperature Dehydration, Isotope Effects, and Influence of Local Surface Structure. *J. Phys. Chem. C* **2007**, *111*, 11059–11067.
44. Henderson, M. A. The Interaction of Water with Solid Surfaces: Fundamental Aspects Revisited. *Surf. Sci. Rep.* **2002**, *46*, 5–308.
45. Li, Z.; Smith, R. S.; Kay, B. D.; Dohnálek, Z. Determination of Absolute Coverages for Small Aliphatic Alcohols on TiO_2(110). *J. Phys. Chem. C* **2011**, *115*, 22534–22539.
46. Perdew, J. P.; Burke, K.; Ernzerhof, M. Generalized Gradient Approximation Made Simple. *Phys. Rev. Lett.* **1996**, *77*, 3865–3868.
47. Lippert, G.; Hutter, J.; Parrinello, M. A Hybrid Gaussian and Plane Wave Density Functional Scheme. *Mol. Phys.* **1997**, *92*, 477–487.
48. VandeVondele, J.; Krack, M.; Mohamed, F.; Parrinello, M.; Chassaing, T.; Hutter, J. QUICKSTEP: Fast and Accurate Density Functional Calculations Using a Mixed Gaussian and Plane Waves Approach. *Comput. Phys. Commun.* **2005**, *167*, 103–128.
49. Goedecker, S.; Teter, M.; Hutter, J. Separable Dual-Space Gaussian Pseudopotentials. *Phys. Rev. B* **1996**, *54*, 1703–1710.
50. VandeVondele, J.; Hutter, J. Gaussian Basis Sets for Accurate Calculations on Molecular Systems in Gas and Condensed Phases. *J. Chem. Phys.* **2007**, *127*, 114105.
51. Grimme, S. Semiempirical GGA-Type Density Functional Constructed with a Long-Range Dispersion Correction. *J. Comput. Chem.* **2006**, *27*, 1787–1799.
52. Dudarev, S. L.; Botton, G. A.; Savrasov, S. Y.; Humphreys, C. J.; Sutton, A. P. Electron-Energy-Loss Spectra and the Structural Stability of Nickel Oxide: An LSDA+U Study. *Phys. Rev. B* **1998**, *57*, 1505–1509.
53. Borodin, A.; Reichling, M. Characterizing TiO_2(110) Surface States by Their Work Function. *Phys. Chem. Chem. Phys.* **2011**, *13*, 15442–15447.
54. Yim, C. M.; Pang, C. L.; Thornton, G. Oxygen Vacancy Origin of the Surface Band-Gap State of TiO_2(110). *Phys. Rev. Lett.* **2010**, *104*, 036806.
55. Mills, G.; Jonsson, H.; Schenter, G. K. Reversible Work Transition-State Theory - Application to Dissociative Adsorption of Hydrogen. *Surf. Sci.* **1995**, *324*, 305–337.
56. Henkelman, G.; Uberuaga, B. P.; Jonsson, H. A Climbing Image Nudged Elastic Band Method for Finding Saddle Points and Minimum Energy Paths. *J. Chem. Phys.* **2000**, *113*, 9901–9904.
57. Marcus, R. A.; Sutin, N. Electron Transfers in Chemistry and Biology. *Biochim. Biophys. Acta* **1985**, *811*, 265–322.
58. Deskins, N. A.; Dupuis, M. Electron Transport *via* Polaron Hopping in Bulk TiO_2: A Density Functional Theory Characterization. *Phys. Rev. B* **2007**, *75*, 195212.
59. Chen, H. N.; Ratner, M. A.; Schatz, G. C. Time-Dependent Theory of the Rate of Photo-Induced Electron Transfer. *J. Phys. Chem. C* **2011**, *115*, 18810–18821.
60. Hutter, J. Excited State Nuclear Forces from the Tamm-Dancoff Approximation to Time-Dependent Density Functional Theory within the Plane Wave Basis Set Framework. *J. Chem. Phys.* **2003**, *118*, 3928–3934.
61. Wu, Q.; Van Voorhis, T. Extracting Electron Transfer Coupling Elements from Constrained Density Functional Theory. *J. Chem. Phys.* **2006**, *125*, 164105.
62. Schmidt, J. R.; Shenvi, N.; Tully, J. C. Controlling Spin Contamination Using Constrained Density Functional Theory. *J. Chem. Phys.* **2008**, *129*, 114110.